Effects of Thin Metal Outer Case and Top Air Gap on Thermal IR Images of Buried Antitank and Antipersonnel Land Mines

Khalil Khanafer, Kambiz Vafai, and Brian A. Baertlein, *Member, IEEE*

***Abstract*—A numerical simulation is carried out to study the effect of the thin metal outer case of an antitank mine and the top air gap of an antipersonnel mine on the passive infrared imaging signature. In addition, an antipersonnel surface mine is also analyzed in the present investigation to show its effect on the soil thermal content. The effect of short- and long-wavelength radiation as well as the convective heat transfer is incorporated in this analysis. The temporal development of the temperature distribution over a diurnal cycle is presented for both buried mines. The results show that the thin metal outer case of a buried antitank mine and the top air space of a buried antipersonnel mine have a pronounced effect on the depthwise temperature through the soil. Also, the results show that both buried mines have a noticeable effect on the intensity of the landmine signature on the soil-top surface over a diurnal cycle. A nonexisting mine signature on the soil-top surface is established for an antitank mine with a thin metal outer case. An almost nonexistent signature is also in evidence for the antipersonnel mine with or without an air gap. The results of the present investigation show that the thermal signature of a surface mine produces much larger temperature extremes than the thermal signature of a buried mine. These results play an important role in producing more effective techniques for mine imaging detection.**

***Index Terms*—Blind mine signature, buried mines, flat soil surface, infrared imaging signature, thin metal outer case, top air gap, very shallow buried mine.**

I. Introduction

THE GOAL of any mine detection method is to achieve a high probability of detection while at the same time maintaining a low probability of false alarm. It is particular important in land mine detection to minimize the time and the cost required to clean up a land mine site. There are several methods, which either have been used or have been proposed for use in land mine detection. These methods include various types of ground-penetrating radar, acoustic sounding, nuclear magnetic resonance, nuclear quadropole resonance, X-rays, trace gas detection, and infrared (IR) detection methods. A number of these applications have limited use due to their inherent shortcomings.

Thermal IR imaging techniques have been the subject of interest for more than a decade now. This interest stems from its importance in mine detection as well as its use in a variety of other applications including the detection of defects in engineering materials, detection of thermal leaks in power plants, and environmental remote sensing [1]. Recent advances in the application of IR imaging techniques have led to successful implementation of these techniques for the detection of buried landmines under suitable conditions.

The IR mine detection method is a promising technique in the detection and distinction of landmines from other buried objects, based on the temperature difference between the target and background that generates the target signature. Due to the variations in the thermophysical properties of the soil and the mine, a thermal contrast exists above the mine, and consequently, IR cameras can be used successfully to detect the energy radiated from the surface. Detailed knowledge of different mine signatures under various circumstances provides proper design and operation of mine-detection sensors. The main disadvantage of applying an IR imaging technique for the detection of buried mines is the presence of false indications in thermograms, as well as the strong influence of the environmental conditions on the images. Many experimental studies associated with the detection of landmines were conducted in the literature based on thermal imaging [2]–[11]. The effect of solar heating, soil disturbances, and temporal climate variations are essential in developing any robust landmine detection method. Better knowledge of these effects on the landmine signature is required to properly use demining IR sensors and to interpret IR imagery, consequently avoiding any drawback associated with this technique.

Sudden heating or cooling of a surface by turning on or off radiation flux on the surface was investigated experimentally [1]. This method was used as means of enhancing the detection capability of buried objects using thermal IR imaging.

Detection of minefields using IR sensing and the time-domain treatment method was conducted for antitanks buried mines [12]. The results showed that distinguishing the mines based on the time sequence of the IR images was more reliable than on a single thermogram. The phenomenology of the potential soil temperature gradients and distributions on the surface of the soil induced by both natural sources and buried mine was studied numerically and experimentally [13]. A three-dimensional (3-D) model for the soil temperature distribution was assumed in that study. The inclusion of a simple vegetation layer in a one-dimensional (1-D) terrain temperature model for thermal IR signature prediction was investigated numerically as well as experimentally [14]. Vegetation was assumed to be a

Manuscript received March 25, 2002; revised October 14, 2002. This work was supported by Lockheed Martin Company under Award QK8822/DAAL01-96-2-0001.

K. Khanafer and K. Vafai are with the Department of Mechanical Engineering, University of California, Riverside, CA 92521 USA.

B. A. Baertlein is with the Department of Electrical Engineering, The Ohio State University, Columbus, OH 43210 USA.

Digital Object Identifier 10.1109/TGRS.2002.807755

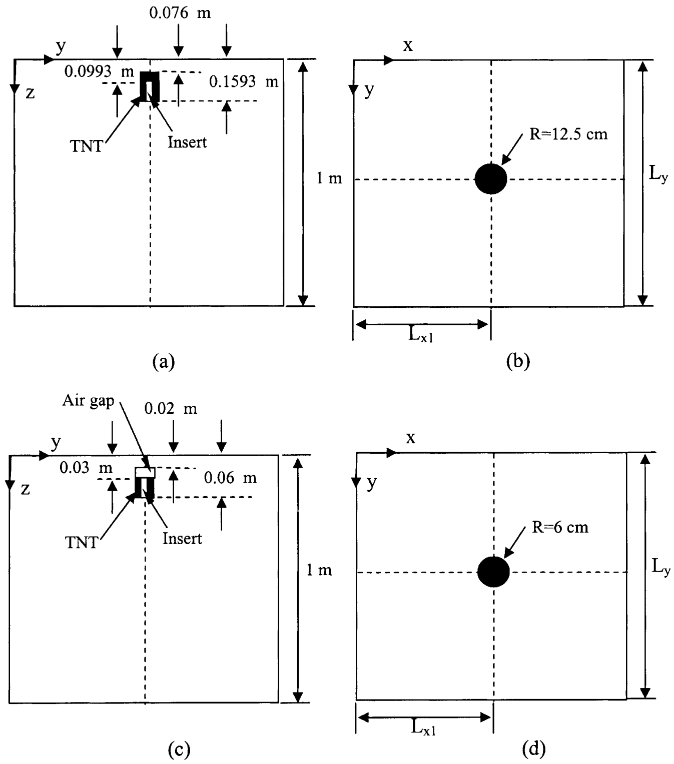

Fig. 1. (a) Sectional view of the antitank mine and the insert object. (b) Top view of the antitank mine. (c) Sectional view of an antipersonnel mine and the insert object. (d) Top view of the buried antipersonnel mine ($L_y = 2L_{x1} = 2$ m).

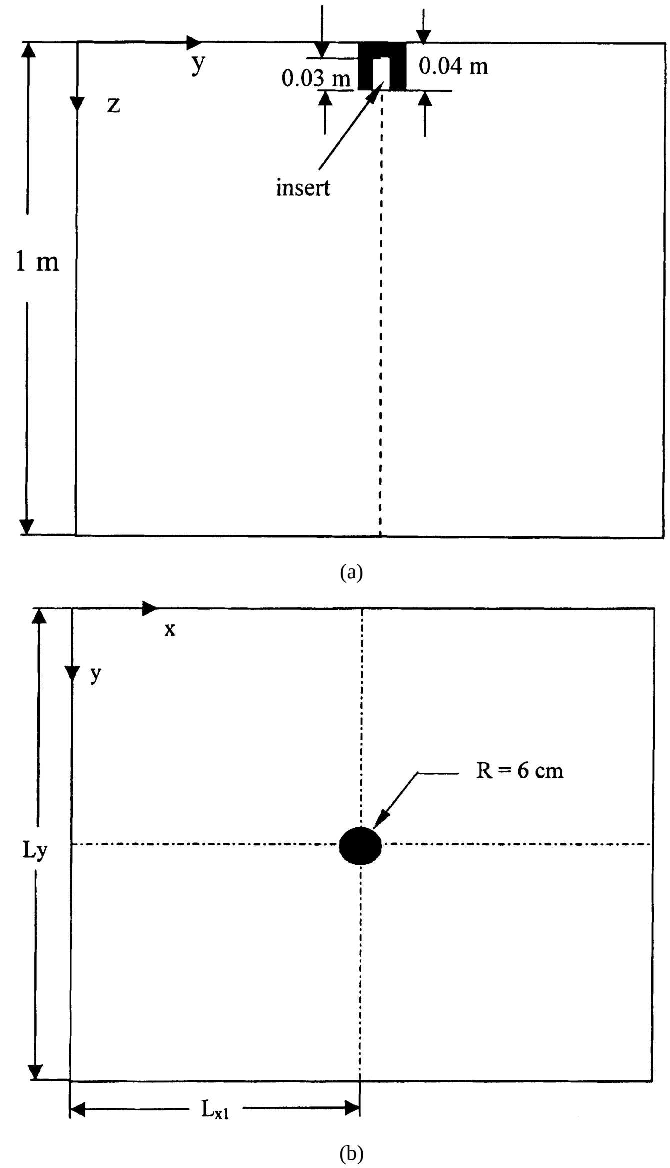

Fig. 2. (a) Sectional view of the surface antipersonnel mine and the insert object. (b) Top view of the surface antipersonnel mine ($L_y = 2L_{x1} = 2$ m).

horizontally homogeneous but porous layer partially covering a specified ground surface. The effect of the vegetation on the remotely sensed temperature was analyzed in that study.

A preliminary 3-D study was conducted to illustrate the effect of the buried landmines on the surface temperature distribution [15]. In this study, the authors showed that the effect of landmines on the structure of the soil's temperature could not be determined using a 1-D model due to the 3-D heat transfer through the soil and the mine. Numerical simulation of thermal signatures of buried mines over a diurnal cycle was developed to study the passive IR signature of a land mine buried under a rough soil surface [16]. A finite element model (FEM) was used to describe the thermal phenomena, including temporal variations, the spatial structure of the signature, and environmental effects. Recently, a comprehensive study on the thermal analysis of buried landmines over a diurnal cycle is conducted under three different soil surface conditions [17]. The occurrence of false readings was established in this study.

Cases of mines maybe made from metal, plastic, fiberglass, or even wood [19]. Another aim of the present study is to investigate thoroughly the effect of the presence of a thin metal outer case around an antitank mine compared to a nonmetallic outer case antitank mine on the soil temperature distribution. In addition, the effect of the presence of an air gap over the TNT material of antipersonnel mine compared to a nonair gap antipersonnel mine will also be investigated. The effect of the surface land antipersonnel mine on the soil surface temperature will be explored in the present study. A 3-D thermal model for soil containing the buried landmine over a diurnal cycle will be incorporated in the present research work. The present study aims at the enhancement of the performance of the IR imagery method through a rigorous analysis of these pertinent effects that influence the function of IR imagery system. Therefore, the present study can play a significant role to develop more robust signal processing techniques.

II. Mathematical Formulation

A. Governing Equations

A surrogate antitank mine and antipersonnel mine buried beneath the soil are used in this study as shown in Figs. 1 and 2. An antipersonnel surface mine is also considered in this study as shown in Fig. 3. The 3-D nature of the thermal interaction within the soil, the insert, the TNT, the air gap region, and the thin metal outer case are accounted for, while the moisture content is assumed to be negligible in this study [1], [5]. The resulting governing equations for the soil, the insert, the TNT, the

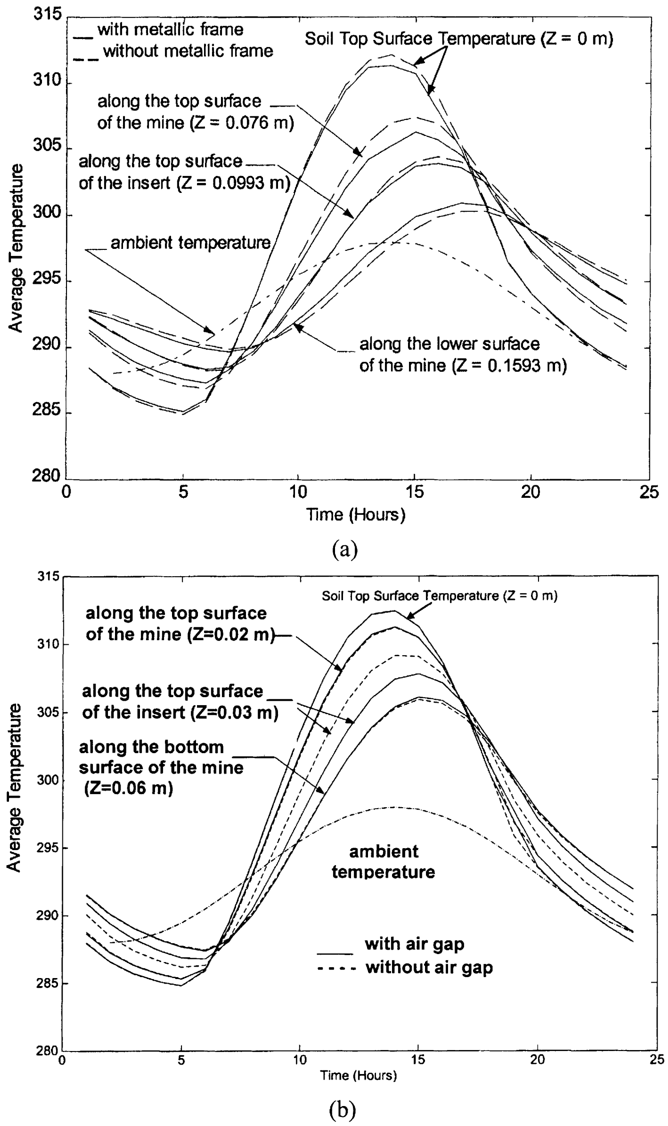

Fig. 3. Comparison between the ambient temperature (K) and the temporal variation of the soil average temperature (K) at various depths. (a) Antitank mine. (b) Antipersonnel mine.

thin metal outer case, and the air gap region can be written as follows:

soil:

$$\frac{\partial}{\partial t}(\rho c T)_s = \nabla(k\nabla T)_s \tag{1}$$

insert:

$$\frac{\partial}{\partial t}(\rho c T)_I = \nabla(k\nabla T)_I \tag{2}$$

TNT:

$$\frac{\partial}{\partial t}(\rho c T)_m = \nabla(k\nabla T)_m \tag{3}$$

thin metal outer case:

$$\frac{\partial}{\partial t}(\rho c T)_f = \nabla(k\nabla T)_f \tag{4}$$

air gap region:

$$\frac{\partial}{\partial t}(\rho c T)_a = \nabla(k\nabla T)_a \tag{5}$$

TABLE I
SPECIFICATION OF TNT MATERIAL

Mine Type	D mm	H mm	k W/m.K	C J/kg.K	ρ kg/m^3
Anti-Tank	250	83.3	0.223442	1289.29	1560
Anti-Personnel	120	40	0.223442	1289.29	1560

TABLE II
SPECIFICATION OF THE INSERT (PLASTIC)

Mine Type	D mm	H mm	k W/m.K	C J/kg.K	ρ kg/m^3
Anti-Tank	40	60	0.5	1260	1760
Anti-Personnel	40	30	0.5	1260	1760

TABLE III
SPECIFICATION OF THE SOIL (SANDY GRAVEL)

k W/m.K	c J/kg. K	ρ kg/m^3
2.5116	837.2	2000

where ρ, c, k, and T are the density, specific heat, thermal conductivity, and temperature, respectively. The subscripts, s, I, m, f, and a denote the soil, insert, mine, thin metal outer case, and the air gap region, respectively. The boundary conditions for the above-mentioned equations can be summarized as follows:

1) soil surface:

$$\vec{n} \cdot k_s \nabla T_s = q_{\text{net}} \tag{6}$$

2) insert surface:

$$\vec{n} \cdot k_I \nabla T_I = \vec{n}.k_m \nabla T_m \tag{7}$$

3) mine surface:

$$\vec{n} \cdot k_s \nabla T_s = \vec{n}.k_f \nabla T_f \tag{8}$$

4) deep soil below the mine:

$$T_S \rightarrow T_\infty \tag{9}$$

where $\vec{n}$ represents the normal unit vector; T_∞ is the deep soil temperature below the buried mine; and q_{net} is the net heat flux into the top surface of the soil and is given by the following expression:

$$q_{\text{net}} = q_{\text{conv}} + q_{\text{sun}} + q_{\text{sky}} - q_{\text{emis}} - q_{\text{evap}} \tag{10}$$

where q_{con} is the convective heat transfer between the surface of the soil and the atmosphere, and q_{sun} is the incident solar energy reduced by cloud cover, atmospheric absorption, albedo, and the cosine of the zenith angle. The sky brightness with a small correction for cloud cover is represented by q_{sky}; q_{emis} is the gray body emission from the soil's surface; and q_{evap} is the latent cooling of the ground caused by evapotranspiration and condensation. In this study, the soil is assumed to be dry, and therefore q_{evap} is set to zero in this model. Convective heat transfer between the soil and the surrounding air is given by

$$q_{\text{conv}} = A_s h(T_{\text{air}} - T_s) \tag{11}$$

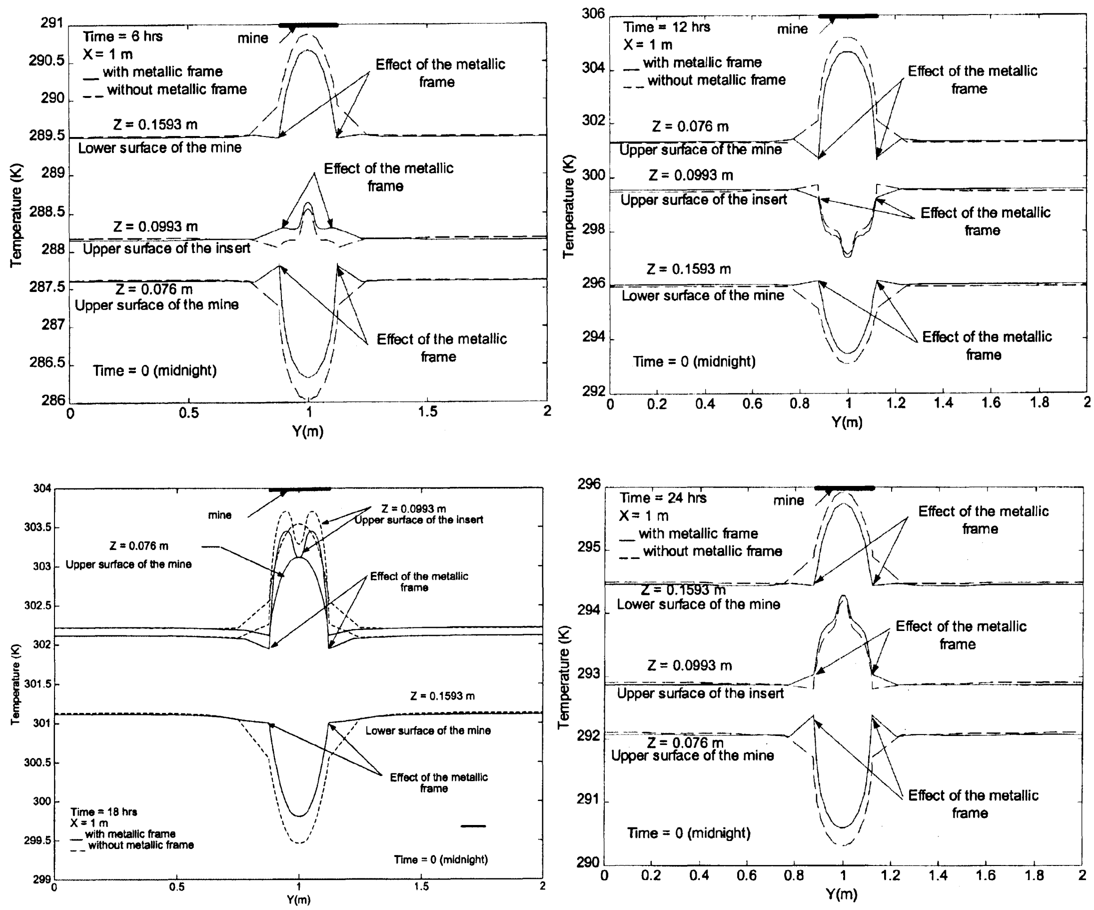

Fig. 4. Temporal variation of the temperature at various depths of the soil with and without a thin metal outer case.

where h is the convective heat transfer coefficient ($h = 5\,\mathrm{W/m^2K}$ based on the typical average wind speed of 2 m/s), and A_s is the exposure surface area. The ambient temperature variation is imposed as [20]

$$T_{\mathrm{air}} = 293 - 5\cos\left(\frac{2\pi(t-2)}{24}\right) \tag{12}$$

where t is given in hours (starting from midnight). The sky irradiance based on the long-wavelength radiation downward from the atmosphere can be expressed as

$$q_{\mathrm{sky}} = \sigma\varepsilon A_s T_{\mathrm{sky}}^4 \tag{13}$$

where $\sigma = 5.67 \times 10^{-8}\,\mathrm{W/m^2K^4}$ is the Stephan–Boltzman constant; ε is the mean emissivity of the surface; and T_{sky} is the effective sky radiance temperature given by [20]

$$T_{\mathrm{sky}} = 0.9 \times T_{\mathrm{air}}. \tag{14}$$

The long-wave radiation emission from the ground's surface is given by the following equation:

$$q_{\mathrm{emis}} = \sigma\varepsilon A T_s^4 \tag{15}$$

where T_s is the soil's surface temperature, and ε is the soil emissivity ($\varepsilon = 0.95$).

The short-wavelength incident solar radiation can be expressed as follows:

$$q_{\mathrm{sun}} = (1 - C_L)S_o(1 - C)M(\phi)\cos(\phi) \tag{16}$$

where $C_L(= 0.2)$ is the cloud cover; $C(= 0.3)$ is the ground albedo; and $S_o(= 1385\,\mathrm{W/m^2})$ is the solar constant. $M(\phi)$ is the approximate atmospheric transmissivity and is given as [20]

$$M(\phi) = 1 - 0.2\cos(\phi)^{-0.5} \tag{17}$$

where ϕ is the zenith angle and can be determined from the following expression:

$$\Pi = \cos\lambda\cos\delta\left(-\cos\left(\frac{2\pi t(h)}{24}\right) + \sin\lambda\sin\delta\right) \Rightarrow \begin{pmatrix}\cos(\phi) = \Pi \text{ if } \Pi > 0\\ \cos(\phi) = 0 \text{ if } \Pi < 0\end{pmatrix} \tag{18}$$

where λ is the local latitude $(= 45^\circ)$ and δ is the declination and is given by

$$\delta = -23.43^\circ\cos\left(\frac{2\pi\,\mathrm{month}}{12}\right). \tag{19}$$

The initial condition for (1)–(5) corresponds to typical conditions and is given as

$$T_s = T_m = T_I = T_a = 293\ \mathrm{K}. \tag{20}$$

B. Numerical Scheme

A Galerkin-based FEM is employed to solve the governing equations in this study. The application of this procedure is well documented [21]. The algebraic equations resulting from the discretization of the governing equations are solved using the

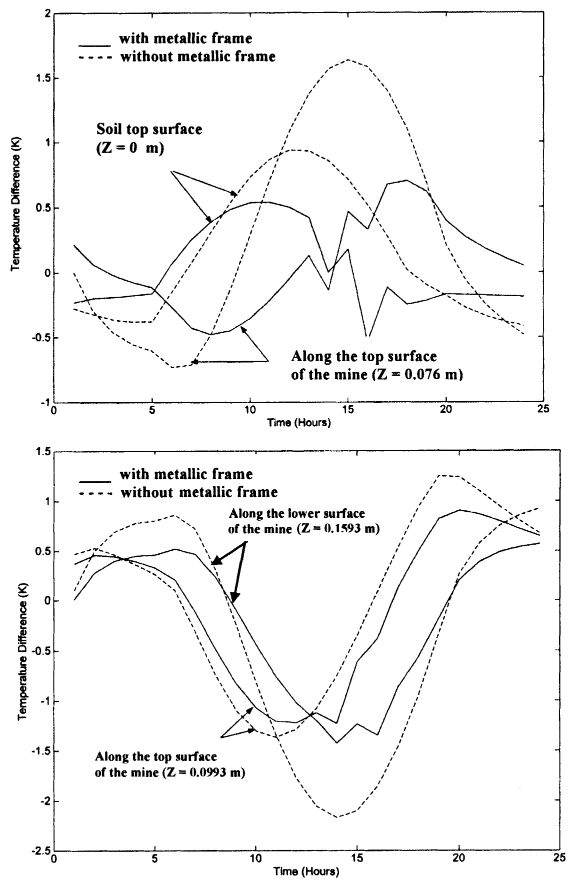

(a)

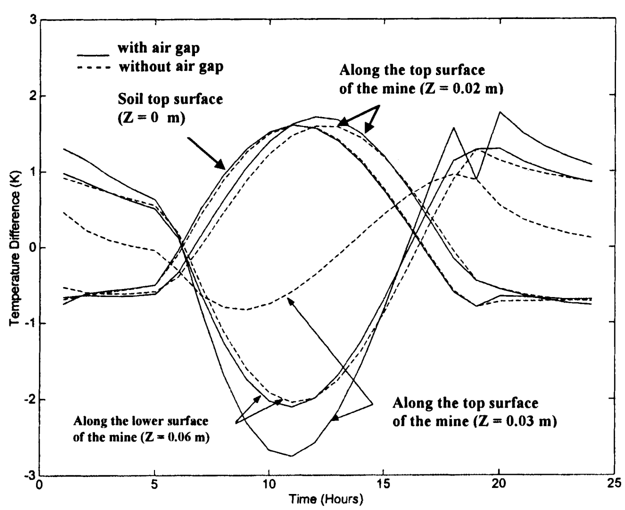

(b)

Fig. 5. Temperature difference between the temperature over different sections of the soil including the mine and the homogenous soil for (a) an antitank mine and (b) an antipersonnel mine.

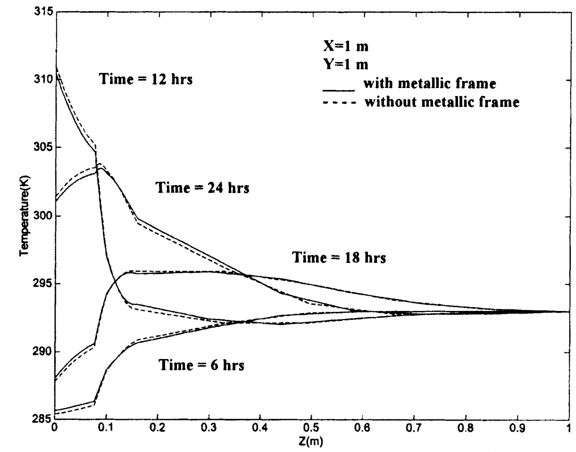

(a)

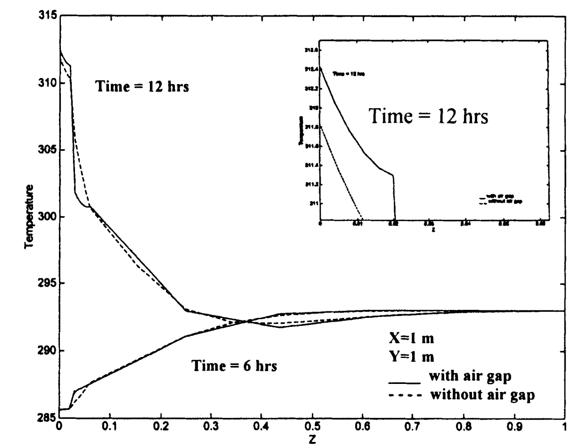

(b)

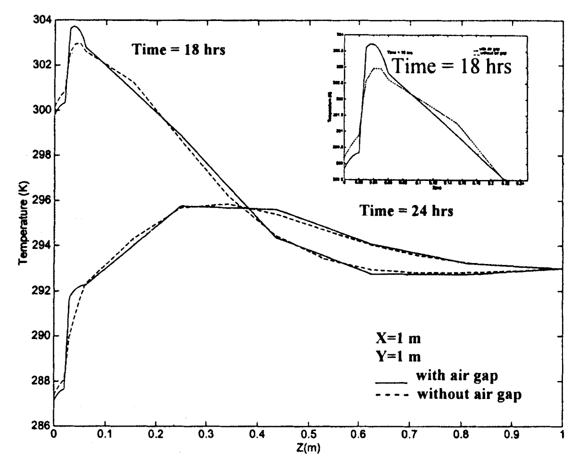

(c)

Fig. 6. Temperature variation at different depths of the soil (a) for an antitank mine, (b) for an antipersonnel mine ($t = 6$ and 12 h), and (c) an antipersonnel mine ($t = 18$ and 24 h).

segregated solution algorithm. The segregated approach solves each conservation equation separately in a sequential segregated manner. This approach is guaranteed to have substantially reduced disk storage requirement compared to the fully coupled approach. The advantage of using this method is that the global system matrix is decomposed into smaller submatrices and then solved in a sequential manner using either direct Gaussian elimination or conjugate-gradient-type schemes. This technique will result in considerably fewer storage requirements. Extensive numerical experimentation was performed to attain grid-independent results for all the field variables. A variable time step was implemented successfully in this model without any loss in the accuracy of the results. One diurnal cycle (24 h) typically took about 48 h on an SGI Octane Workstation. There was a significant increase in the CPU time in order to increase the accuracy and to reduce the tolerance.

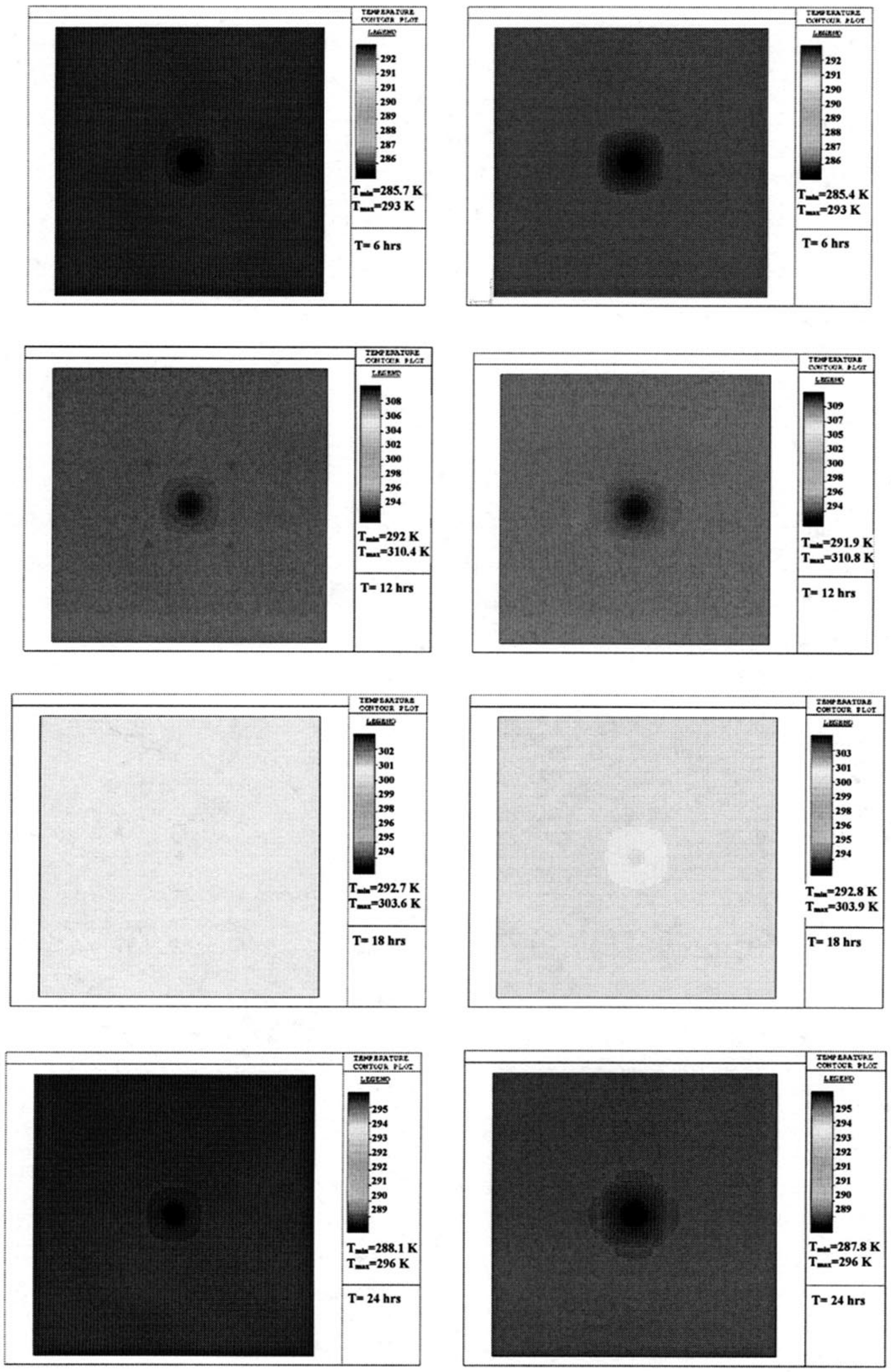

(a) (b)

Fig. 7. Comparison of the top surface temperature for the buried antitank mine at various periods of time (a) with a thin metal outer case and (b) without a thin metal outer case.

III. Discussion of Results

Mines may be found on the surface, partially covered by soil or vegetation, or buried beneath the soil at some depth. In this study, two different types of mines are studied, namely antipersonnel and antitank mines. These two classes of mines, while being the most pertinent and relevant kind in the area of buried mines, also cover a wide spectrum of geometrical and thermophysical differences among the mines. In addition, the effect of using a thin metal outer case for a buried antitank mine on the IR signature is investigated. Moreover, the effect of the presence of the top air gap on the mine signature of an antipersonnel buried mine is also studied in the present investigation. A surface antipersonnel land mine is also considered in the present research work. For this purpose, a flat surface for the soil is assumed in the present research work. A simulant antitank mine buried beneath the soil with an outer steel case as shown in Fig. 1(a) and (b) is used in this study. For the buried antipersonnel mine, the

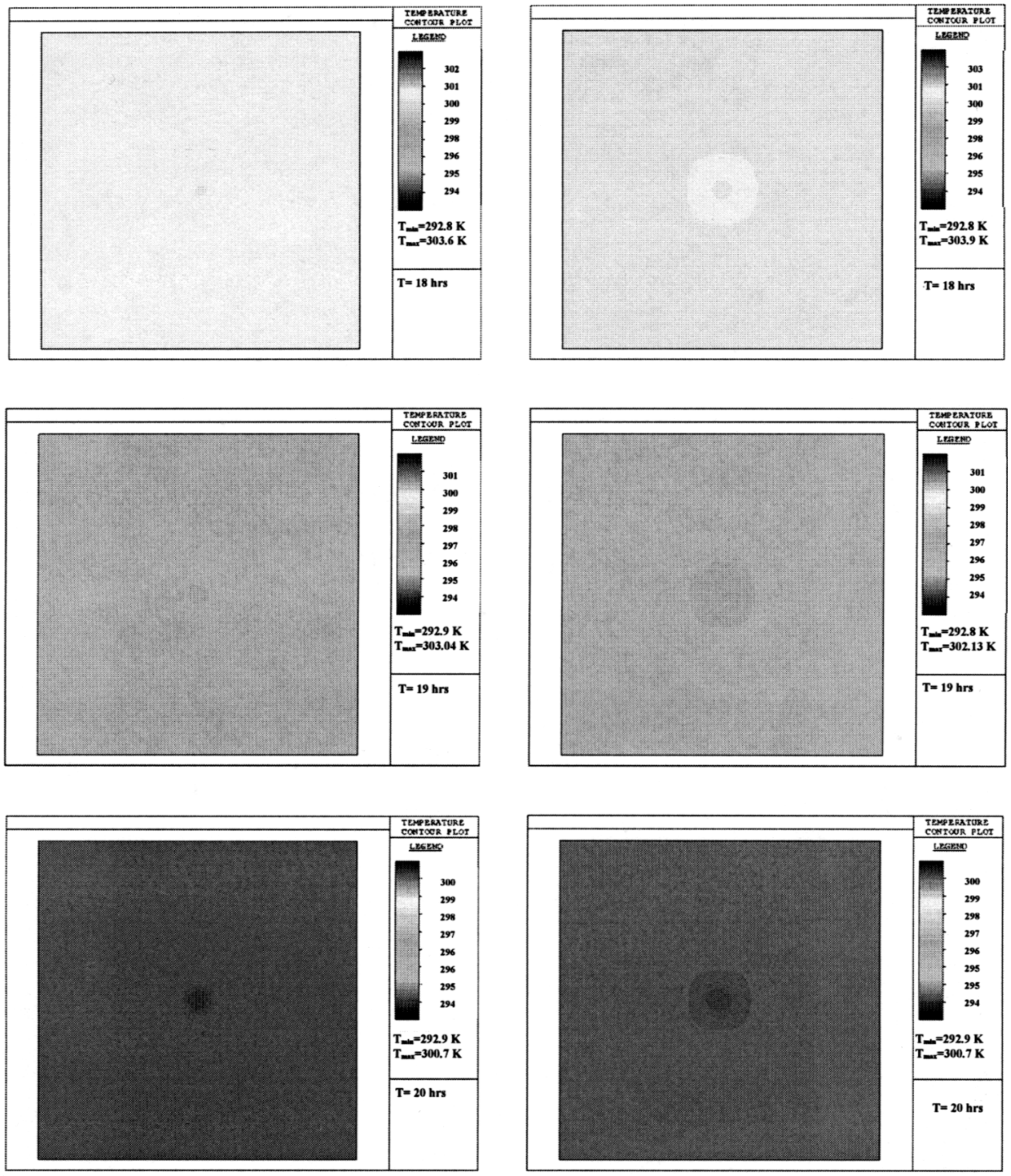

(a) (b)

Fig. 8. Comparison of the critical blind mine spot for the buried antitank mine (a) with a thin metal outer case and (b) without a thin metal outer case.

typical burial depth and typical diameter of the mine are shown in Fig. 1(c) and (d). It should be noted that the top part of the antipersonnel mine is filled with air. Both mines are modeled as a homogenous object of circular shape having the same thermal properties as that of TNT. Typical dimensions of the mines and the insert used in this investigation are shown in Figs. 1 and 2. The thermophysical properties of the soil, insert, antitank mine, and antipersonnel mine are tabulated in Tables I–III.

This study does not include any quantitative comparison with practical measurements, due to the lack of experimental results in the literature that show the effect of the thin metal outer case of the buried antitank mine and the top air gap of an antipersonnel mine on the temporal variation of the soil temperature. We did consider some variation in the parameters representing the soil to account for variations in the soil conditions. The results of the present investigation were compared qualitatively with the experimental results reported in the literature [12]. The comparison was found to be in good agreement with the main features of the experimental results.

A. Effect of the Buried Antitank and Antipersonal Mines on the Temporal Temperature Variation of the Soil at Various Depths

The effect of the presence of the mine on the temporal average temperature of the soil at various depths is depicted in Fig. 3 for both buried mines. For the buried antitank mine, Fig. 3(a) shows a comparison of the soil average temperature at various depths with and without a thin outer metal case. Fig. 3(a) shows that

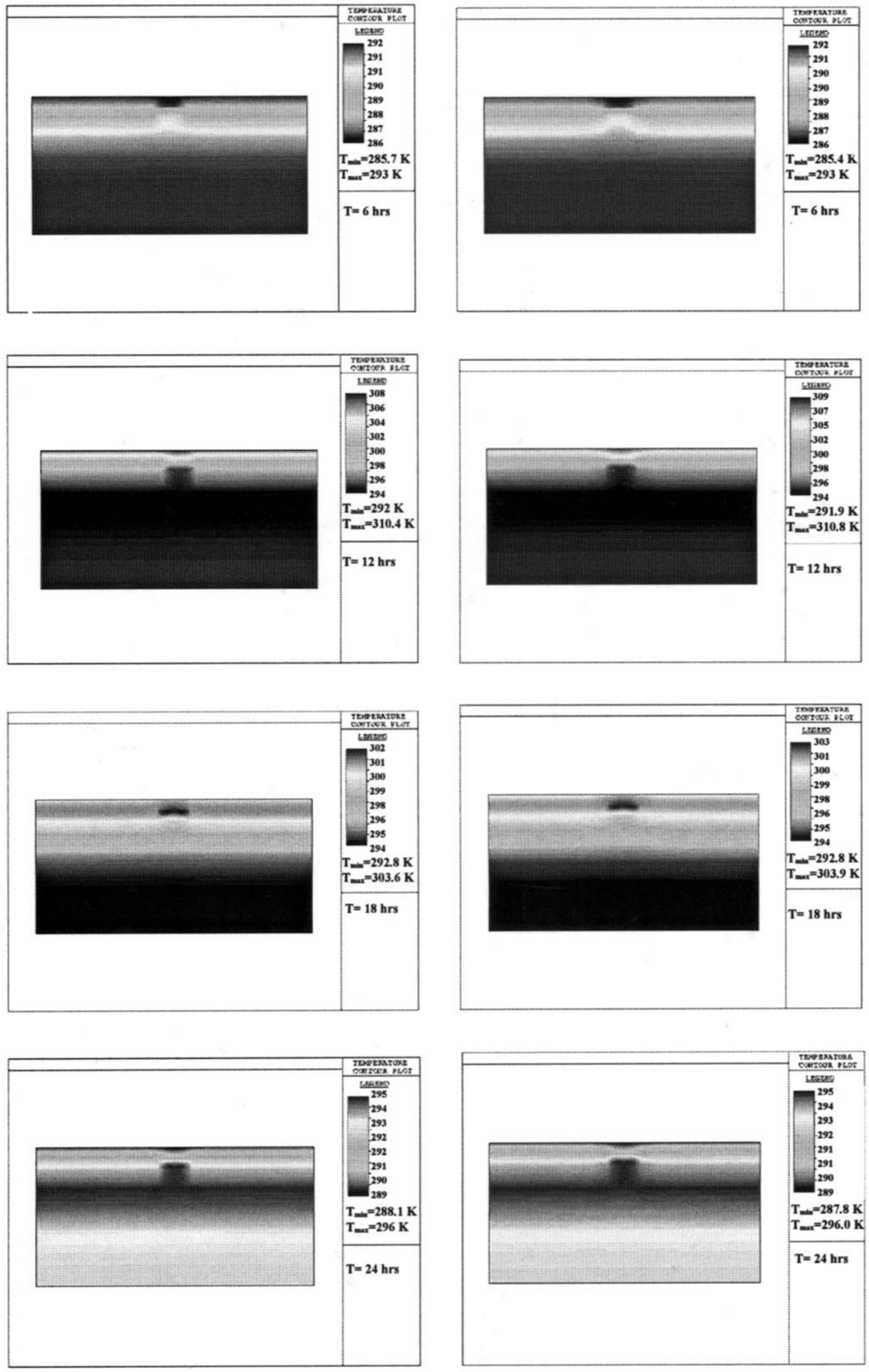

(a) (b)

Fig. 9. Comparison of the depthwise temperature distribution for the buried antitank mine at various periods of time (a) with a thin metal outer case and (b) without a thin metal outer case.

there is a relatively slight discrepancy between the two situations as a result of high thermal conductivity of the thin metal outer case. The effect of the top air gap of an antipersonnel buried mine on the temporal average temperature at various depths compared to the ambient temperature is also illustrated in Fig. 3(b). Fig. 3(b) shows the existence of a large discrepancy in the average temperature along the top surface of the insert compared with other soil depths between cases where the air gap is considered and when it is neglected. This difference can be attributed to poor thermal conductivity of the air gap compared to the thermal conductivity of other materials around the top surface of the insert. For both buried mines, there is a large variation in the temperature between the ambient temperature and the temperature at different depths of the soil. This can be attributed essentially to the effect of the solar radiation.

The effect of the thin metal outer case of the buried antitank mine on the temporal variation of the temperature at various depths of the soil is shown in Fig. 4. It can be seen from this

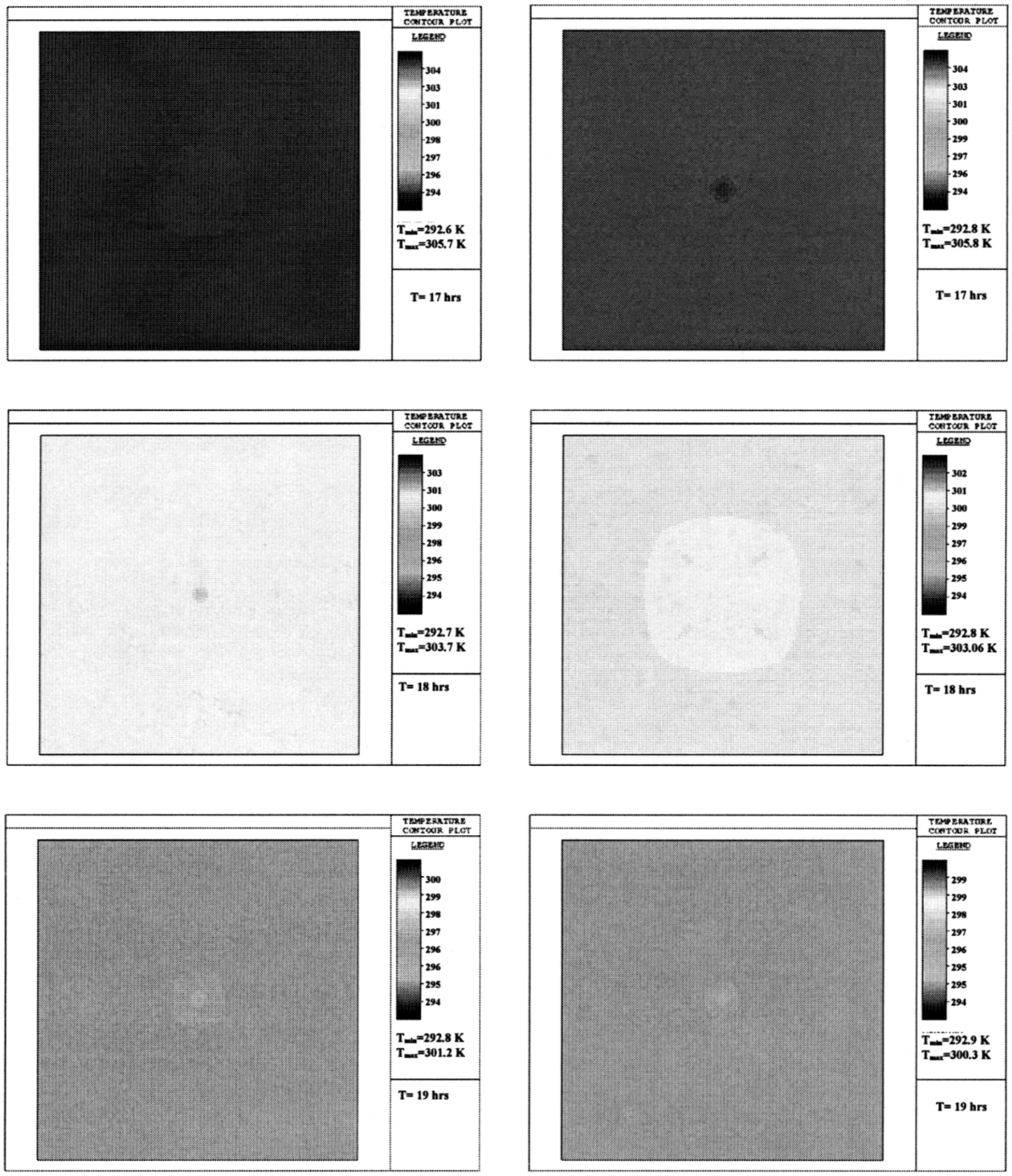

(a) (b)

Fig. 10. Critical blind mine spot for the buried antipersonnel mine (a) with an air gap and (b) without an air gap.

figure that the thin metal outer case has a significant effect on the temperature distribution compared to the nonmetal outer case mine over a diurnal cycle. This effect is due to an appreciable difference in the thermal conductivity of the thin metal outer case compared to the thermal conductivity of the TNT material. This difference creates a large change in the temperature in the vicinity of the interface between the two materials as depicted in this figure. Moreover, high conducting material leads to a high heat transfer by conduction mode resulting in a higher temperature difference between the two cases. This effect is more pronounced with respect to the mine temperature signal $(\Delta T(t) = T_m(t) - T_{nm}(t))$ as shown in Fig. 5(a). The subscripts m and nm refer to the temperature distribution in the presence and absence of a mine, respectively. This figure presents a detailed picture on the effect of the thin metal outer case on the mine temperature signal over a diurnal cycle. Fig. 5(a) shows that there is a significant difference in the mine temperature signal on the soil surface for a mine with a thin metal outer case and one without it. This difference is more noticeable around noon time where the incident solar energy reaches its highest value. The effect of the top air gap on the temperature difference between the presence of the buried mine and the homogeneous soil at different depths of the soil is clearly shown in Fig. 5(b). This effect is significant only over the insert where the air gap is located. This is due to the fact that the area above the insert, which is filled with air, has poor thermal contacts between the insert and the surroundings. The spikes shown in Fig. 5 are related to the different response times between the temperature of the

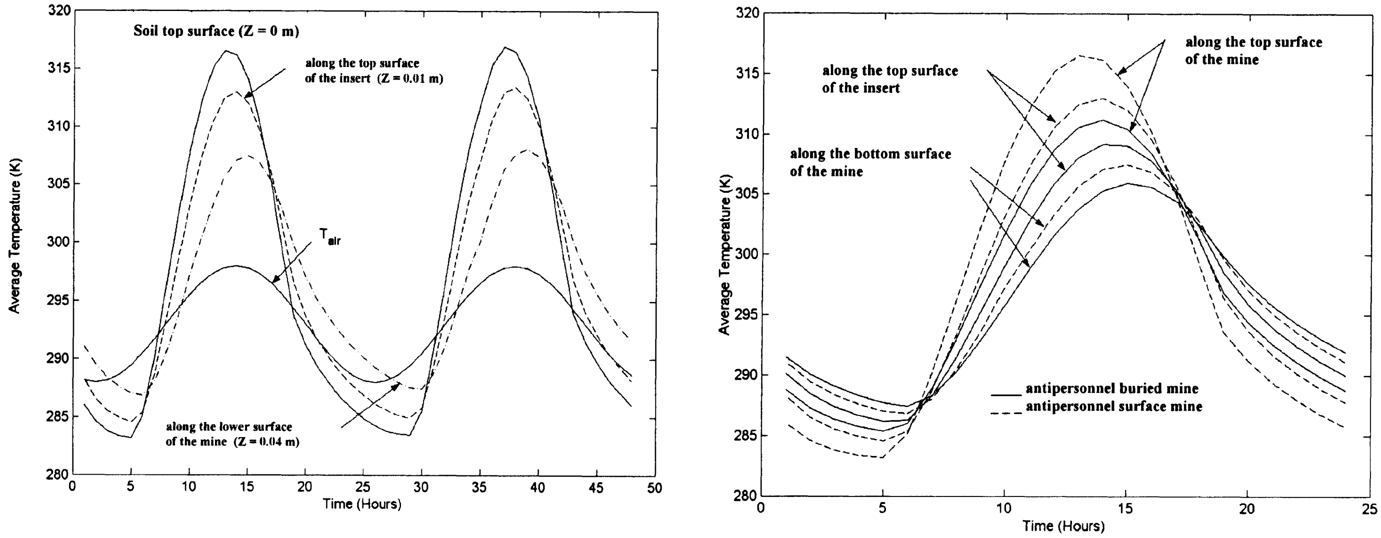

(a) (b)

Fig. 11. (a) Comparison between the temporal variations of the average soil temperature beneath surface mine at various depths and the ambient temperature. (b) Comparison of the average temperature between the antipersonnel surface mine and the buried antipersonnel mine over a diurnal cycle at various depths.

homogenous soil and the temperature of the soil in the presence of the mine. These different response times lead to a phase angle shift and can be partially observed in Fig. 3. The phase angle shift is a result of the effect of different thermophysical properties between the mine and the homogeneous soil. As mentioned before, this difference in the thermophysical properties can lead to a significant change in the soil temperature distribution.

The effect of the thin metal outer case and the top air gap on the depthwise temperature along the centerline (i.e., a line passing vertically through the center of the mine) of both buried mines is illustrated in Fig. 6. For the antitank mine, the difference in temperature for both the metallic and nonmetallic outer frames is almost negligible in the depth direction of the soil as depicted in Fig. 6(a). In addition, over a period of 12 h, it can be seen from Fig. 6(b) that the soil-top surface temperature reaches its highest value compared with other periods of time. This is due to the effect of the direct incident solar energy into the soil surface. As the time advances, the surface temperature decreases, and the mine temperature increases due to the downward heat conduction. For the antipersonnel buried mine, Fig. 6(c) shows that the top air gap has a more pronounced effect on the depthwise temperature variation at large periods of time within a given cycle. Over a period of 12 h, there is a more appreciable temperature difference between the two situations. This can be attributed to the fact that the air gap, which has low thermal conductivity compared to the thermal conductivity of a nonair gap, tends to resist the heat flow downward and as a result reduces the speed of the transfer of the short-wavelength radiation by conduction through the soil and consequently through the mine. Over the first 6-h period of the cycle, this effect is not pronounced due to the negligible effect of the solar incident energy into the soil until dawn. As the time proceeds (Time = 18 h), the temperature distribution reverses in such way that the temperature for the case with the air gap is higher than the case without air gap. This can be attributed mainly to the presence of an air gap region, which has a lower thermal conductivity causing an additional resistance to the heat transfer as compared to the case without air gap (higher thermal conductivity).

B. Effect of the Buried Antitank Mine on Both the Soil Signature Intensity and the Temporal Depthwise Temperature Distribution

Fig. 7 displays the variation in the antitank mine signature intensity at different periods of time for both cases (i.e., with and without a thin metal case). It is evident from Fig. 7 that the landmine signature contrast varies substantially over time. Both cases have a similar temperature distribution pattern on the top surface of the soil. An interesting situation observed in Fig. 8, points to the nonexisting landmine signature (time = 19 h) on the top surface of the soil for both cases. This nonexisting signature occurs due to the convergence of the soil surface and the ambient temperatures as depicted in Fig. 3 [Fig. 5(a), left side shows it clearly]. Identification of this type of nonexisting landmine signature requires information regarding the temperature variations beneath the soil surface. Alternatively, temporal information regarding the landmine signature on the soil surface can resolve this critical time line. This can be achieved by sweeping the site mine using the IR technique at different periods of time based on the model results, to bypass the nonexisting signature situation on the soil surface.

Fig. 9 shows the variation of depthwise temperature distribution at different time periods for the antitank buried mine with and without a thin metal outer case. It can be seen that both cases follow the same trend at different times. Fig. 9 provides a clear picture of the effect of the mine on the soil depthwise temperature distribution for both cases. It can be seen from Fig. 9 that the mine tends to block the conductive heat transfer through the soil beneath the mine until dawn where the effect of the short-wavelength sun radiation is negligible. For later times, the soil-top surface temperature rises due to the effect of the incident sun radiation on the soil surface, and consequently, more heat is transferred by conduction into the soil layer above the mine. This effect continues up to 3 h from noon. Thereafter, the mine acts as a heat sink until sunset at which time it starts to transfer heat downward by conduction through the soil during the night while the soil temperature above the mine cools promptly due to the effect of radiation from the soil-top surface.

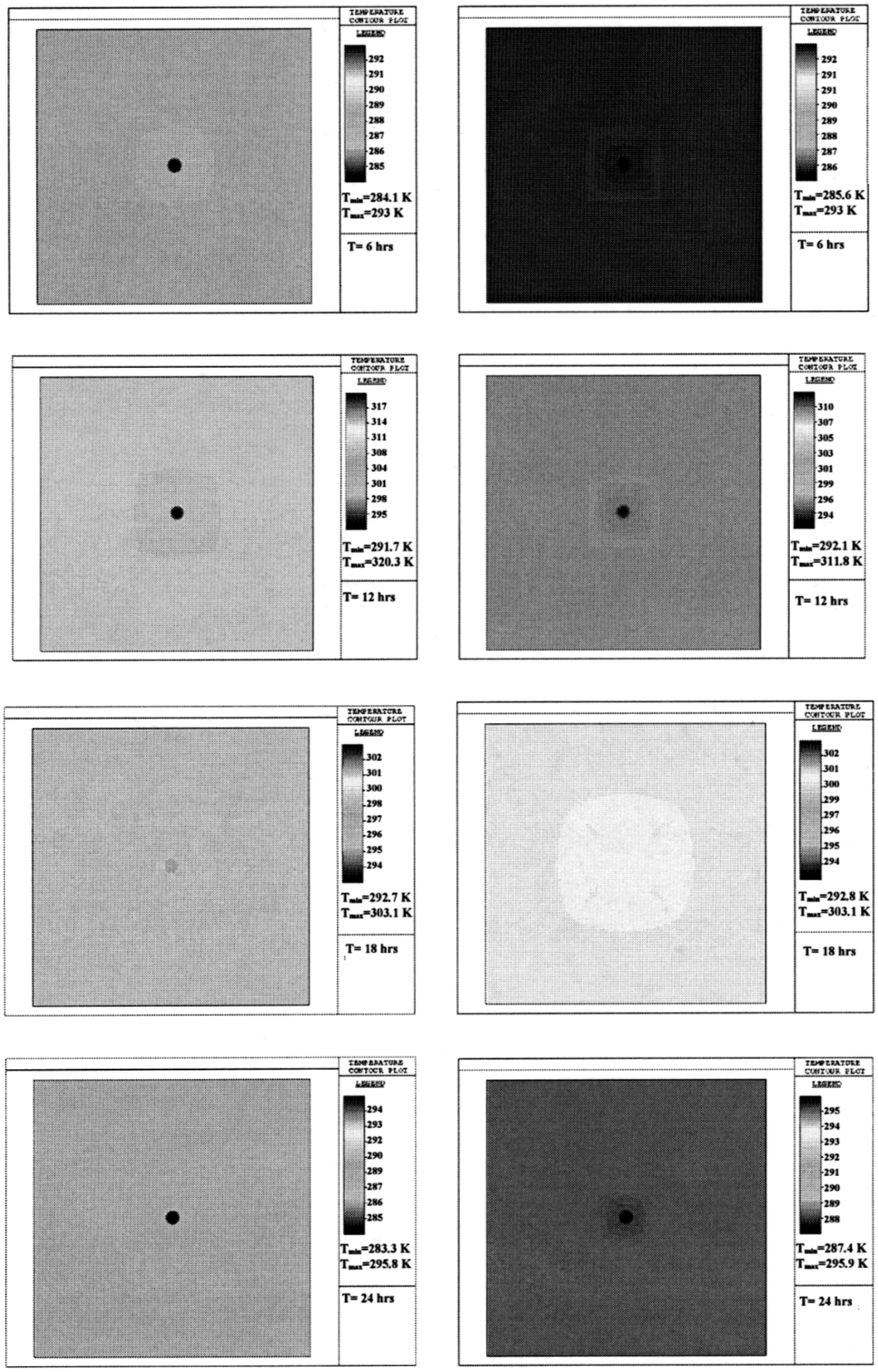

(a) (b)

Fig. 12. Comparison of the mine signature on the soil surface at various periods of time (a) for an antipersonnel surface mine and (b) for a buried antipersonnel mine.

C. Effect of an Antipersonnel Mine on the Nonexisting Mine Signature on the Soil-Top Surface

A remarkable result is observed for both situations (i.e., with and without an air gap) of the buried antipersonnel mine, which is the possibility of the occurrence of the nonexisting mine signature on the top surface of the soil as shown in Fig. 10. In this case, the signature does not totally vanish as in the case of the antitank mine. This is due to the fact that the antipersonnel mine is buried at shallow depth (2 cm), which allows higher heat interaction between the mine and the soil's top surface. However, the signature is faded to a degree that makes it quite hard to detect.

D. Effect of the Surface Mine on the Thermal Content of the Soil

The antipersonnel surface mine is also studied in this investigation to show its effect on the performance of the IR ther-

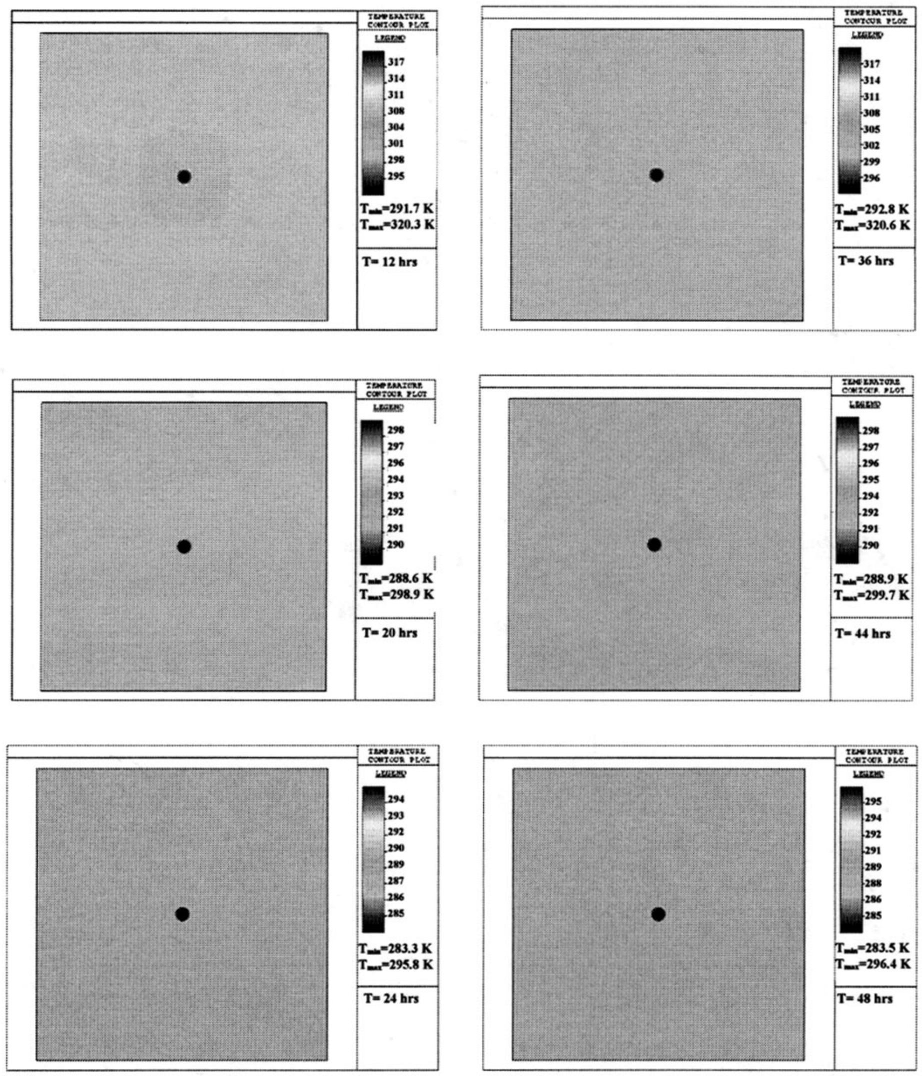

Fig. 13. Periodicity of the soil-top surface temperature distribution of the surface antipersonnel mine over a diurnal cycle.

mographic detection of the buried objects, as well as on the thermal content of the soil beneath the mine. Fig. 11(a) shows the temporal variation of the average temperature taken at different depths of the soil over two diurnal cycles. A comparison of the average temperature between the antipersonnel surface mine and antipersonnel buried mine over a diurnal cycle at various depths is shown in Fig. 11(b). This figure shows that the surface mine has a significant effect on the temperature of the top soil surface compared to mines buried beneath the soil surface. This can be attributed to more rapid changes on the top surface of the mine due to external radiation. A comparison of the mine signature on the soil-top surface between the surface mine and the buried mine is shown in Fig. 12. The thermal IR signature of the surface mine is characterized by the diurnal dependence on the incident solar radiation as well as energy transfer due to convection and radiation. Thus, it can be seen from this figure that the surface mine is at a higher temperature at noon (time $= 12$ h) compared to the buried mine at the same time.

The surface mine has more direct interaction with the surroundings compared to the buried mine. As a result, the surface mine also has the lowest surface temperature at midnight (time $= 24$ h) compared to the buried mine as shown in Fig. 12. The thermal signature of the surface mine has a similar diurnal dependence as that of the buried mine. However, the difference between the two is in terms of temperature variations. The buried mine has a more subdued range of temperature variations compared to that of surface mine.

The periodicity of the present results is illustrated in this investigation for the surface mine as shown in Fig. 13. It can be clearly seen from this figure that the temperature pattern repeats itself over a diurnal cycle. The reason for the existence of this periodicity is due to the fact that the transient effects die out after the passage of an initial period, which is typically of the order of 12 h.

IV. Conclusion

The results of the present study show that the outer metallic frame of an antitank and the top air gap of an antipersonnel buried mine have a significant effect on the soil temperature distribution, as well as on the intensity of the landmine signature on the soil-top surface over a diurnal cycle. Interesting blind spots are established on the top soil surface for antitank and antipersonnel buried mines. Moreover, a shallow buried mine and surface mine do not produce blind spots over the soil surface, while deeper buried mines do. The present results show that the thermal signature of a surface mine produces larger temperature extremes than the thermal signature of a buried mine.

REFERENCES

[1] P. Li, A. Maad, F. Moshary, M. F. Arend, and S. Ahmed, "Infrared imaging of buried objects by thermal step-function excitations," *Appl. Opt.*, vol. 34, pp. 5809–5816, 1995.

[2] L. A. LeSchack and N. K. Del Grande, "A dual-wavelength thermal infrared scanner as a potential airborne geophysical exploration tool," *Geophysics*, vol. 41, pp. 1318–1336, 1976.

[3] Y. H. Janssen, A. N. Jong, H. Winkel, and F. J. Putten, "Detection of surface laid and buried mines with IR and CCD cameras, an evaluation based on measurements," *Proc. SPIE*, vol. 2765, pp. 448–459, Apr. 1996.

[4] G. Maksymomko, B. Ware, and D. Poole, "A characterization of diurnal and environmental effects on mines and the factors influencing the performance of mine detecting ATR algorithms," *Proc. SPIE*, vol. 2496, pp. 140–151, Apr. 1995.

[5] J. R. Simard, "Improved landmine detection capability (ILDC): Systematic approach to the detection of buried mines using passive IR imaging," *Proc. SPIE*, vol. 2765, pp. 489–500, Apr. 1996.

[6] B. A. Barbour, M. W. Jones, H. B. Barnes, and C. P. Lewis, "Passive IR polarization sensors: A new technology for mine detection," *Proc. SPIE*, vol. 3392, pp. 96–103, 1996.

[7] M. Larive, L. Collot, S. Breugnot, H. Botma, and P. Roos, "Laid and flush-buried mines (sic) detection using 8–12 μm polarimetric imager," *Proc. SPIE*, vol. 3392, pp. 115–120, 1996.

[8] M. Larive, D. Spoliansky, and O. Trezieres, "Pre-processing of 8–12 μm polarimetric features for laid and flush-buried mines detection," *Proc. SPIE*, vol. 3710, no. 1, pp. 197–202, Apr. 1999.

[9] C. DiMarzio, T. Vo-Dinh, and H. E. Scott, "Some approaches to infrared spectroscopy for detection of buried objects," *Proc. SPIE*, vol. 3392, pp. 158–166, 1996.

[10] A. Filippidis, L. C. Jain, and N. Martin, "Using genetic algorithms and neural networks for surface land mine detection," *IEEE Trans. Signal Processing*, vol. 47, pp. 176–186, Jan. 1999.

[11] N. Stacy, R. Smith, and G. Nash, "Automatic target recognition for the ingarra airborne radar surveillance system," DSTO, Microwave Radar Div., Int. Rep., Aug. 1994.

[12] P. Pregowski and W. Swiderski, "Detection of minefields using IR sensing and time-domain treatment method," *Proc. SPIE*, vol. 3079, pp. 791–800, Apr. 1997.

[13] P. Pregowski, W. Swiderski, R. T. Walczak, and K. Lamorski, "Buried mine and soil temperature prediction by numerical model," *Proc. SPIE*, vol. 4038, pp. 1392–1403, 2000.

[14] L. K. Balick, R. K. Scoggins, and L. E. Link, "Inclusion of a simple vegetation layer terrain temperature models for thermal IR signature prediction," *IEEE Trans. Geosci. Remote Sensing*, vol. GE-19, pp. 143–152, July 1981.

[15] B. A. Baertlein, K. Khanafer, and K. Vafai, "Analysis and modeling of thermal IR signatures of buried land mines," in *Proc. 4th Annual Conf. Advanced Sensors Consortium (ASC)*, 2000.

[16] I. K. Sendur and B. A. Baertlein, "Numerical simulation of thermal signatures of buried mines over a diurnal cycle," *Proc. SPIE*, vol. 4038, pp. 156–167, Apr. 2000.

[17] K. Khanafer and K. Vafai, "Thermal analysis of buried land mines over a diurnal cycle," *IEEE Geosci. Remote Sensing*, vol. 40, pp. 461–473, Feb. 2002.

[18] A. J. Wilkinson and M. R. Inggs, "Radiometry for landmine detection," *Proc. 1998 South African Symp. on Communications and Signal Processing—COMSIG '98*, pp. 477–482, Sept., 7–8 1998.

[19] A. W. England, "Radiobrightness of diurnally heated freezing soil," *IEEE Trans. Geosci. Remote Sensing*, vol. 28, pp. 464–474, July 1990.

[20] C. W. Allen, *Astrophysical Quantities*. London, U.K.: Athlone, 1963, p. 127.

[21] *FIDAP Theoretical Manual*, Fluid Dynamics Int., Evanston, IL, 1990.

Khalil Khanafer received the B.S. degree and the M.S. degree in mechanical engineering from Kuwait University, Safat, Kuwait, in 1993 and 1997, respectively. He received the Ph.D. degree in mechanical engineering from The Ohio State University, Columbus, in 2002.

He is currently a Post Doctorate in the Department of Mechanical Engineering, University of California, Riverside. His interests include fluid flow and heat transfer in porous medium, cooling of electronic equipment, natural convection in open-ended enclosures, and nanotechnology.

Kambiz Vafai received the B.S. degree in mechanical engineering from the University of Minnesota, Minneapolis, in 1975, and the M.S. and Ph.D. degrees in mechanical engineering, both from the University of California, Berkeley, in 1977 and 1980, respectively.

His current research interests include transport through porous media, multiphase transport, natural convection in complex configurations, analysis of porous insulations, heat flux applications, free surface flows, flat-shaped heat pipes, and power electronics. He has conducted basic and applied research in several areas related to heat and mass transfer, such as fundamental aspects of transport through porous media, natural convection in open-ended configurations, condensation and phase change, multiphase transport through porous media, and flow and heat transfer in the brake housing of an aircraft. He has been the Editor-in-Chief of the *Journal of Porous Media* since 1997. Also, he is on the editorial advisory boards of several international journals in the field of heat and mass transfer.

Dr. Vafai has won various awards and has been an Invited Professor at universities in France, Germany, and Italy. He has held a Presidential Chair Professorship at the University of California, Riverside. He has been a Fellow of the American Society of Mechanical Engineers since 1992, an Associate Fellow of the American Institute of Aeronautics and Astronautics since 1998, and a Fellow of the American Association for the Advancement of Science.

Brian A. Baertlein (S'88–M'89) received the Ph.D. degree in electrical engineering from the University of Arizona, Tucson, in 1988.

He is currently a Research Scientist and Adjunct Associate Professor of electrical engineering at the ElectroScience Laboratory, The Ohio State University (OSU), Columbus. Before joining OSU, he was a Senior Scientist with several small businesses doing work for the U.S. Department of Defense and Department of Energy. His recent research has addressed detection of land mines using a variety of sensors, multisensor data fusion, radar system analysis, and modeling of electromagnetic phenomena in magnetic resonance imaging. Prior work includes studies of electromagnetic scattering and propagation phenomena, antennas, and electromagnetic compatibility.

Dr. Baertlein is a member of Eta Kappa Nu, Tau Beta Pi, ACES, SPIE, and SAE.